

RESEARCH ARTICLE

10.1002/2014JA020092

Key Points:

- The outer radiation belt can be created from a low-energy source alone
- Chorus acceleration is effective from the plasmopause to the magnetopause
- In active conditions radial diffusion depletes the outer belt

Correspondence to:

S. A. Glauert,
sagl@bas.ac.uk

Citation:

Glauert, S. A., R. B. Horne, and N. P. Meredith (2014), Simulating the Earth's radiation belts: Internal acceleration and continuous losses to the magnetopause, *J. Geophys. Res. Space Physics*, 119, 7444–7463, doi:10.1002/2014JA020092.

Received 16 APR 2014

Accepted 20 AUG 2014

Accepted article online 26 AUG 2014

Published online 23 SEP 2014

Simulating the Earth's radiation belts: Internal acceleration and continuous losses to the magnetopause

Sarah A. Glauert¹, Richard B. Horne¹, and Nigel P. Meredith¹

¹British Antarctic Survey, Natural Environment Research Council, Cambridge, England

Abstract In the Earth's radiation belts the flux of relativistic electrons is highly variable, sometimes changing by orders of magnitude within a few hours. Since energetic electrons can damage satellites it is important to understand the processes driving these changes and, ultimately, to develop forecasts of the energetic electron population. One approach is to use three-dimensional diffusion models, based on a Fokker-Planck equation. Here we describe a model where the phase-space density is set to zero at the outer L^* boundary, simulating losses to the magnetopause, using recently published chorus diffusion coefficients for $1.5 \leq L^* \leq 10$. The value of the phase-space density on the minimum-energy boundary is determined from a recently published, solar wind-dependent, statistical model. Our simulations show that an outer radiation belt can be created by local acceleration of electrons from a very soft energy spectrum without the need for a source of electrons from inward radial transport. The location in L^* of the peaks in flux for these steady state simulations is energy dependent and moves earthward with increasing energy. Comparisons between the model and data from the CRRES spacecraft are shown; flux dropouts are reproduced in the model by the increased outward radial diffusion that occurs during storms. Including the inward movement of the magnetopause in the model has little additional effect on the results. Finally, the location of the low-energy boundary is shown to be important for accurate modeling of observations.

1. Introduction

Since the discovery of the Earth's radiation belts about 55 years ago [Van Allen and Frank, 1959; Van Allen, 1959], considerable progress has been made on understanding their structure and behavior. However, many significant questions remain, particularly about their behavior during geomagnetic storms. Typically in the radiation belts, the high-energy (>100 keV) electrons are trapped in two torus-shaped regions; the inner belt lies between about 1.5 and 2 Earth radii from the center of the planet and the outer belt between about 3 and 7 Earth radii. The inner electron belt is relatively stable, but the outer belt is very dynamic. This variability is ultimately determined by the solar wind interacting with the magnetosphere [Paulikas and Blake, 1979; Baker et al., 1986, 1994, 1997; Li et al., 1997; Reeves et al., 1998; Miyoshi and Kataoka, 2005], and the flux of relativistic electrons in the outer belt can vary by several orders of magnitude on timescales from minutes to weeks [e.g., Blake et al., 1992; Baker et al., 1994].

At any time, the structure of the belts depends on transport, loss, and acceleration processes all of which vary with the solar wind and geomagnetic conditions [Thorne et al., 2005a; Horne et al., 2006; Thorne, 2010]. The behavior of the belts under any particular set of conditions is determined by the combined effect of the different processes. For example, it has been shown that at a fixed L shell, 50% of geomagnetic storms increase the relativistic electron flux by to within a factor of 2, 20% decrease it, while the remainder leave it unchanged [Reeves et al., 2003]. It is important to understand the behavior of the radiation belts since relativistic electrons damage satellites [Wrenn, 1995; Baker, 2001; Wrenn et al., 2002; Lucci et al., 2005] and are a risk to humans in space. Modeling the electron flux provides a useful tool for scientists and satellite designers, and forecasting the electron flux is valuable for spacecraft operators.

One method that has been employed successfully to simulate the high-energy electron radiation belts involves solving a three-dimensional Fokker-Planck equation [Schulz and Lanzerotti, 1974] to determine the evolution of the phase-averaged phase-space density [Beutier and Boscher, 1995; Subbotin and Shprits, 2009; Su et al., 2010; Albert et al., 2009; Glauert et al., 2014]. These models can include various processes such as radial transport across the magnetic field, pitch angle and energy diffusion by wave-particle

interactions, Coulomb collisions with atmospheric gases, and magnetopause shadowing [Su et al., 2011; Shprits et al., 2013].

Radial diffusion transports electrons across the geomagnetic field and plays an important role in the Earth's radiation belts [Roederer, 1970]. It is driven by large-scale fluctuations of the magnetic and electric fields at frequencies comparable to the drift period of the electrons, around a few mHz [Falthammar, 1965]. It can be enhanced by ULF waves [Hudson et al., 1999; Elkington, 2006; Mathie and Mann, 2000] driven by fast solar wind flows along the magnetopause which propagate inside the magnetosphere to lower L^* . Radial diffusion conserves the first two adiabatic invariants, but it breaks the third. When the gradient in phase-space density is outward, radial diffusion is inward and can lead to significant energization. If the phase-space density gradient is inward, the resulting outward radial diffusion can transport electrons to the magnetopause where they are lost [Shprits et al., 2006]. Adiabatic effects during storms have also been demonstrated to produce additional losses to the magnetopause [Kim et al., 2011b].

Gyroresonant wave-particle interactions with ELF/VLF waves play a significant role in the dynamics of the radiation belts. These interactions break the first and second adiabatic invariants, causing pitch angle and energy diffusion [Kennel and Petschek, 1966]. Electrons trapped in the radiation belts may encounter several different types of ELF/VLF electromagnetic wave as they orbit the Earth. Whistler mode chorus waves may be present on the dawnside, outside the plasmasphere, particularly during active conditions [e.g., Meredith et al., 2001, 2003a, 2012; Li et al., 2009, 2011]. These waves can interact strongly with electrons with energies from a few electron volts up to several MeV across a range of L shells from the plasmapause out to $L = 10$ and can cause both loss and acceleration of relativistic electrons [Horne et al., 2005a, 2005b, 2013b; Thorne et al., 2005b; Bortnik and Thorne, 2007]. In regions of low plasma density these interactions are particularly effective, leading to acceleration of the trapped particle population [Summers et al., 1998; Meredith et al., 2002; Horne et al., 2003]. The losses tend to dominate at low energies, typically a few keV to a few hundred keV, but at higher energies, generally > 500 keV, wave acceleration is usually dominant [Horne et al., 2013b]. However, the energy at which the transition occurs between dominant losses and dominant acceleration varies, since both loss and acceleration depend upon the plasma density and the wave properties, which in turn depend on the location and level of geomagnetic activity. Plasmaspheric hiss, found inside the plasmasphere and in plasmaspheric plumes, is responsible for the formation of the slot region between the inner and outer radiation belts [Lyons and Thorne, 1973; Meredith et al., 2007, 2009] and the quiet time decay of energetic electrons in the outer radiation belt [Meredith et al., 2006; Summers et al., 2007; Lam et al., 2007]. Lightning-generated whistlers (LGW) may influence loss rates deep inside the slot region [Abel and Thorne, 1998a, 1998b; Meredith et al., 2009].

There is growing evidence that magnetopause shadowing is an important loss process for the radiation belts causing flux dropout events [e.g., Bortnik et al., 2006; Shprits et al., 2006; Ukhorskiy et al., 2006; Ohtani et al., 2009; Saito et al., 2010; Turner et al., 2012a]. Dropouts are characterized by a decrease of several orders of magnitude in the electron flux over a period of a few hours, seen over a range of L shells, energies, and pitch angles. Although adiabatic effects may play a part, recent results have shown that dropouts include the actual loss of electrons [Turner et al., 2012a]. These losses may be due to a combination of the inward movement of the magnetopause and outward radial transport, though other mechanisms including wave-particle interactions with electromagnetic ion cyclotron (EMIC) waves causing loss to the atmosphere, current sheet scattering, and nonlinear wave-particle interactions may also play a part [see Turner et al., 2012b, and references therein].

Radial diffusion coefficients have been presented by many authors, beginning with Falthammar [1965]. Diffusion rates parameterized by the geomagnetic index Kp were derived by Brautigam and Albert [2000] and have since been widely used in radiation belt modeling codes [e.g., Varotsou et al., 2005; Albert et al., 2009; Subbotin and Shprits, 2009; Glauert et al., 2014].

Global models of the radiation belts use drift- and bounce-averaged pitch angle and energy diffusion coefficients. For three-dimensional models, these are computed using quasi-linear theory. Chorus waves, in particular, are known to be highly nonlinear due to their short duration rising tone frequency structure [e.g., Omura et al., 2009; Santolik et al., 2014]. However, it is not yet computationally feasible to perform fully nonlinear simulations of chorus waves over the time and spatial scales required by global models. Albert [2010] and Tao et al. [2012] demonstrate that there is remarkable agreement between fully nonlinear and quasi-linear simulations for small-amplitude waves. Fully drift- and bounce-averaged lower band

chorus diffusion coefficients, computed using quasi-linear theory and based on data from the CRRES (Combined Release and Radiation Effects Satellite) spacecraft, were first presented in *Varotsou et al.* [2005] for $2.5 \leq L \leq 6.5$. *Li et al.* [2007] calculated diffusion coefficients due to both plasmaspheric hiss and chorus using parameterized models of the wave properties. Recently, improved models for chorus and plasmaspheric hiss have been published [*Horne et al.*, 2013a; *Glauert et al.*, 2014]. *Horne et al.* [2013a] presented drift- and bounce-averaged diffusion coefficients for upper and lower band chorus waves based on data from seven spacecraft [*Meredith et al.*, 2012], extending the radial coverage to $1.5 \leq L^* \leq 10$. *Glauert et al.* [2014] presented new diffusion coefficients due to plasmaspheric hiss and LGW. These new diffusion coefficients for chorus, plasmaspheric hiss, and LGW have been incorporated into the British Antarctic Survey (BAS) Radiation Belt Model [*Glauert et al.*, 2014].

As well as diffusion coefficients, global models require boundary conditions, typically applying these on the pitch angle, energy or momentum, and L^* boundaries. For the pitch angle, high-energy and low L^* boundaries these are usually straightforward as the phase-space density or its gradient can be set to zero. The low-energy boundary condition may be determined directly from data [e.g., *Albert et al.*, 2009; *Glauert et al.*, 2014] or by assuming that there is a value of the first invariant (where the minimum-energy boundary is placed) where the phase-space density is constant with L^* or time [e.g., *Varotsou et al.*, 2005, 2008; *Subbotin and Shprits*, 2009; *Su et al.*, 2010]. The outer L^* boundary is the most problematic as this boundary usually acts as a time-dependent source for the simulation. If satellite data are not available to determine this boundary condition, then a functional form can be employed. *Varotsou et al.* [2005] used a fixed kappa distribution, and *Shprits et al.* [2006] derived an exponential fit to the flux at $L = 6$ using CRRES data. More recently, *Shin and Lee* [2013] presented three models for the flux at $7.5 R_E$ based on solar wind parameters.

Several authors have included magnetopause shadowing effects in diffusion models. Using a variable phase-space density on the outer boundary, *Brautigam and Albert* [2000], *Miyoshi et al.* [2003, 2006], and *Shprits et al.* [2006] reproduced the behavior of dropouts by suddenly decreasing the phase-space density. This creates a steep gradient in L^* so radial diffusion rapidly depletes the outer belt. *Yu et al.* [2013] simulated dropouts using a one-dimensional radial diffusion code with a variable outer boundary located at the last closed drift shell (LCDS) showing that magnetopause shadowing is the primary loss mechanism during dropout events for $L^* > 5$.

We describe a different approach to setting the outer boundary condition for three-dimensional radiation belt modeling. This approach models the whole outer radiation belt out as far as the magnetopause where the phase-space density is always set to zero. The main source for the system is at the low-energy boundary. This has advantages for forecasting as no data are required on the outer L^* boundary. However, it does require that all the essential physical processes are captured and that the low-energy boundary is well modeled. Here we present initial results using a simple statistical model for the low-energy boundary. We demonstrate that our model can produce an outer belt and that steady state solutions show known features of the radiation belts. To model actual events the location of the LCDS is included in the model, though we show that including the location of the LCDS does not have a dramatic effect on the results presented here. Finally, we discuss the optimum location of the low-energy boundary.

Section 2 describes the BAS Radiation Belt Model and presents the boundary conditions used for this study. Section 3 shows the results of simulating a period of steady conditions starting with an empty radiation belt. In sections 4 and 5 we compare results with data for a specific event and discuss the effect of introducing the location of the LCDS into the model. Section 6 discusses the importance of the location of the minimum-energy boundary. Finally, the results are discussed and our conclusions presented in sections 7 and 8.

2. The BAS Radiation Belt Model

The evolution of the phase-averaged phase-space density $f(p, r, t)$ in the Earth's radiation belts can be described by a diffusion equation [*Schulz and Lanzerotti*, 1974]. In the BAS Radiation Belt Model [*Glauert et al.*, 2014], this equation is transformed to pitch angle, α , energy, E , and $L^* = 2\pi M/(\Phi R_E)$, where Φ is the

third adiabatic invariant, M is the magnetic moment of the Earth's dipole field, and R_E is the Earth's radius. The model solves the equation

$$\begin{aligned} \frac{\partial f}{\partial t} = & \frac{1}{g(\alpha)} \frac{\partial}{\partial \alpha} \Big|_{E,L} \left(g(\alpha) D_{\alpha\alpha} \frac{\partial f}{\partial \alpha} \Big|_{E,L} \right) \\ & + \frac{1}{A(E)} \frac{\partial}{\partial E} \Big|_{\alpha,L} \left(A(E) D_{EE} \frac{\partial f}{\partial E} \Big|_{\alpha,L} \right) \\ & + L^2 \frac{\partial}{\partial L} \Big|_{\mu,J} \left(\frac{D_{LL}}{L^2} \frac{\partial f}{\partial L} \Big|_{\mu,J} \right) - \frac{f}{\tau_L} \end{aligned} \quad (1)$$

where

$$g(\alpha) = T(\alpha) \sin 2\alpha \quad (2)$$

$$A(E) = (E + E_0)(E(E + 2E_0))^{1/2} \quad (3)$$

and E_0 is the electron rest mass energy. $T(\alpha)$ can be approximated by $T(\alpha) = (1.3802 - 0.3198(\sin \alpha + \sin \frac{1}{2} \alpha))$ in a dipole field [Lenchek *et al.*, 1961].

Here L^* has been written as L for simplicity. Similarly, $D_{\alpha\alpha}$, D_{EE} , and D_{LL} are the drift- and bounce-averaged pitch angle, energy, and radial diffusion coefficients respectively but have been written in this way for simplicity. Their units are s^{-1} , $J^2 s^{-1}$, and s^{-1} , respectively. The loss term (f/τ_L) represents losses to the atmosphere due to collisions. The loss timescale, τ_L , is set to one quarter of the bounce time in the loss cone and is infinite elsewhere.

Mixed pitch angle energy diffusion terms have been omitted from equation (1). *Albert and Young* [2005] and *Subbotin et al.* [2010] demonstrate that the mixed diffusion terms have little effect on equatorially mirroring particles; other authors [Tao *et al.*, 2008, 2009] suggest they may have a significant effect. In this study, we only present results for near equatorially mirroring particles so we will omit the mixed diffusion terms.

2.1. Radial Diffusion

Radial diffusion transports electrons across the Earth's magnetic field. It is incorporated into models through the radial diffusion term in equation (1) above. *Brautigam and Albert* [2000] derived the most commonly used form for the radial diffusion coefficients, D_{LL} , [e.g., *Albert et al.*, 2009; *Lam et al.*, 2007; *Subbotin and Shprits*, 2009]. These Kp -dependent diffusion coefficients are defined for Kp values between 1 and 6 and are given by

$$D_{LL} = D_{LL}^M + D_{LL}^E. \quad (4)$$

The two terms D_{LL}^M and D_{LL}^E represent radial diffusion due to magnetic and electric field fluctuations, respectively. D_{LL}^M (with units of per day) is derived from data at $L^* = 4$ and $L^* = 6.6$ and takes the form

$$D_{LL}^M = 10^{0.506Kp - 9.325} L^{*10}. \quad (5)$$

For $L^* > 4$, $D_{LL}^E < D_{LL}^M$, so studies of the outer belt usually omit D_{LL}^E [Miyoshi *et al.*, 2006; Tu *et al.*, 2009]. Additionally, *Kim et al.* [2011a] show that using the electrostatic component, D_{LL}^E , produces unrealistically high fluxes in the slot region, so we have also used

$$D_{LL} = D_{LL}^M. \quad (6)$$

However, *Zhao and Li* [2013] conclude that D_{LL}^M underestimates radial diffusion at low L , so this choice may underestimate the radial diffusion at low L , particularly during active conditions.

2.2. Diffusion From Wave-Particle Interactions

As they drift around the Earth, electrons trapped in the radiation belts meet several different types of electromagnetic wave, including whistler mode chorus, plasmaspheric hiss, and LGW. The wave-particle interactions from these encounters are modeled by the pitch angle and energy diffusion terms in equation (1).

The pitch angle and energy diffusion coefficients due to plasmaspheric hiss and LGW used here are described in *Glauert et al.* [2014]. Using data from the CRRES satellite, drift-averaged wave spectra were

determined for each L , with bin sizes of $0.5L$, for three different levels of Kp , namely, $Kp < 2$, $2 \leq Kp \leq 4$, and $Kp > 4$. Each of these spectra was fitted with three Gaussians to accurately represent them over the frequency range 100 Hz to 5 kHz. Diffusion coefficients were then calculated for each L and Kp value in eight magnetic local time (MLT) bins, each of width 3 h, using a wave-normal angle model that varied with latitude. These MLT-dependent diffusion coefficients were then drift averaged.

Plasmaspheric hiss is seen predominantly within the plasmapause. In our model the plasmapause location can be defined using the models for plasmapause location, L_p , presented in *O'Brien and Moldwin [2003]*. They define

$$L_p = 5.9 - 0.43Kp^m, \quad (7)$$

where Kp^m is the maximum value of Kp over the preceding 36 h, excluding the last 2 h, or

$$L_p = 6.3 - 1.57 \log_{10} |Dst^m|, \quad (8)$$

where Dst^m is the minimum value of the Dst index in the last 24 h. For the steady state simulations in section 3, we use the Kp -based model as this reduces the number of input parameters required. All other simulations use the Dst model. Diffusion due to plasmaspheric hiss is only included in the model inside the plasmapause.

Horne et al. [2013b] presented new pitch angle and energy diffusion coefficients for upper and lower band whistler mode chorus waves. These diffusion rates were calculated using data from seven different satellites to provide frequency spectra for lower and upper band chorus waves for $1.5 \leq L^* \leq 10$ in steps of $0.5L^*$, absolute magnetic latitude $0 \leq |\lambda_m| \leq 60^\circ$ in 6° bins, 3 h MLT bins covering all MLT, and five levels of geomagnetic activity defined by the Kp index, namely $Kp < 1$, $1 \leq Kp < 2$, $2 \leq Kp < 3$, $3 \leq Kp < 4$, and $Kp \geq 4$. To derive the diffusion coefficients, the frequency spectrum for each of upper and lower band chorus in each L^* , latitude, MLT, and geomagnetic activity bin was fitted with a Gaussian distribution. The wave-normal angle distribution was a Gaussian in the tangent of the wave-normal angle, following *Glauert and Horne [2005]*. In each bin, the ratio f_{pe}/f_{ce} was given by a new equatorial model with L^* , MLT, and Kp dependence, based on CRRES and THEMIS (Time History of Events and Macroscale Interactions during Substorms) data [*Horne et al., 2013b*]. Bounce-averaged diffusion rates were calculated in each L^* , latitude, MLT, and geomagnetic activity bin. The results for the separate latitude ranges at each L^* and MLT location were combined to give a diffusion rate averaged over the whole bounce orbit. Drift- and bounce-averaged diffusion rates were then found by averaging the bounce-averaged diffusion rates over MLT. Finally, the drift- and bounce-averaged diffusion rates for lower and upper band chorus were combined. A complete description of this process and the resulting diffusion coefficients is given in *Horne et al. [2013b]*.

Previous chorus models have been based on CRRES data and have been restricted to $L < 6.5$. The use of these new diffusion coefficients extends the use of radiation belt models to the region well beyond geostationary orbit.

Figure 1 shows chorus pitch angle and energy diffusion coefficients for $2 \leq Kp < 3$ at $L^* = 3, 5, 7$, and 9. In these moderate geomagnetic conditions, there is still significant pitch angle and energy diffusion beyond geostationary orbit (roughly $L^* > 6$). Note that, as expected, there is little diffusion at $L^* = 3$ since, for $2 \leq Kp < 3$, this region lies within the plasmasphere where chorus is not often observed.

2.3. Boundary Conditions

Equation (1) is solved for a range of L^* where $L_{\min}^* \leq L^* \leq L_{\max}^*$, for equatorial pitch angles $0^\circ \leq \alpha \leq 90^\circ$ and for a range of energies which depend on L^* . Since the radial diffusion operators in equation (1) act at constant μ and J (the first and second adiabatic invariants), the minimum and maximum energies at L_{\max}^* define the minimum and maximum values of μ or vice versa [*Glauert et al., 2014*]. For the results presented here, the minimum value of μ , μ_{\min} is chosen and the minimum energy, which varies with L^* , determined from that. Except in section 6, we use $\mu_{\min} = 100$ MeV/G which corresponds to an energy of ~ 128 keV at $L^* = 6$ and ~ 30 keV at $L^* = 10$, for an equatorially mirroring electron assuming a dipole field.

The model requires boundary conditions to be supplied on six boundaries, at the minimum and maximum values of pitch angle, energy, and L^* . For these simulations, three of the boundary conditions are the same as those described in *Glauert et al. [2014]*; at $\alpha = 0^\circ$ and $\alpha = 90^\circ$, $\partial f / \partial \alpha = 0$, and at E_{\max} (or μ_{\max}), $f = 0$.

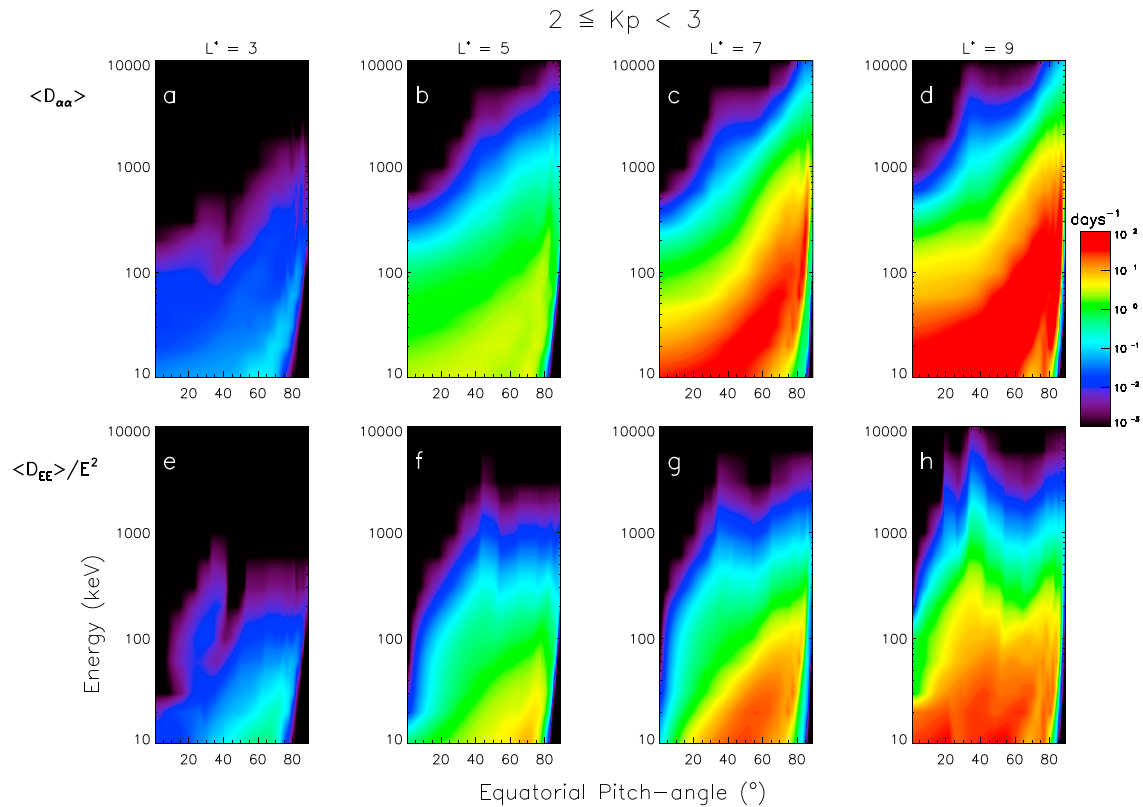


Figure 1. Drift- and bounce-averaged (a–d) pitch angle and (e–h) energy diffusion rates (days^{-1}) due to whistler mode chorus for $2 \leq Kp < 3$ at $L^* = 3, 5, 7,$ and 9 .

The inner boundary, L_{\min}^* , is set at $L_{\min}^* = 2$ and is specified using a Kp -dependent condition derived by averaging CRRES data from before 24 March 1991. The equatorial 90° flux for $1.95 \leq L^* \leq 2.05$ was averaged for three levels of Kp , namely $Kp < 2$, $2 \leq Kp \leq 4$, and $Kp > 4$ for each of the energy channels on the CRRES Medium Electrons A (MEA) instrument. (Since data from the MEA instrument were contaminated by protons at low L following the storm that occurred on 24 March 1991 [Vampola and Korth, 1992], only data collected before this date were used in the averaging for the inner L^* and low-energy boundaries.) More details of the processing of the CRRES data are given in section 4.

Figure 2 shows the resulting 90° flux at $L^* = 2$ for the three different levels of Kp ; the flux shows very little variation with Kp . The flux at other equatorial pitch angles was determined assuming the flux varies as $\sin \alpha$. Due to the presence of the slot region, numerical experiments show that for the simulations presented here, varying the flux on the minimum L^* boundary has no discernable effect on the flux in the outer radiation belt.

The outer boundary, L_{\max}^* , is placed at $L_{\max}^* = 10$. On this boundary we set $f = 0$ for all energies, simulating losses to the magnetopause. This approach differs from previous three-dimensional simulations where the outer boundary generally acts as a source of electrons. In our model, there will always be outward radial diffusion from the outer radiation belt to this boundary.

The main source in the model is the phase-space density on the low-energy boundary. For the results presented here, this boundary is placed at $\mu_{\min} = 100$ MeV/G, except in section 6 where the choice of μ_{\min} is discussed. Varotsou et al. [2008] assume that the phase-space density is constant with L^* along the entire low-energy boundary, which is placed at $\mu_{\min} = 0.1$ MeV/G. Subbotin and Shprits [2009] use a steady state solution for radial diffusion to provide the low-energy boundary condition for their simulations. Since radial diffusion is rapid at larger L^* , this results in a nearly flat radial profile in phase-space density for $L^* > \sim 5.5$ with a much lower phase-space density in the slot region; their choice of μ_{\min} was $\mu_{\min} = 11$ MeV/G. Other authors [e.g., Albert et al., 2009; Glauert et al., 2014] use data for the low-energy boundary condition. However, the model described here is being developed for use in forecasting where using data for the low-energy boundary is not an option.

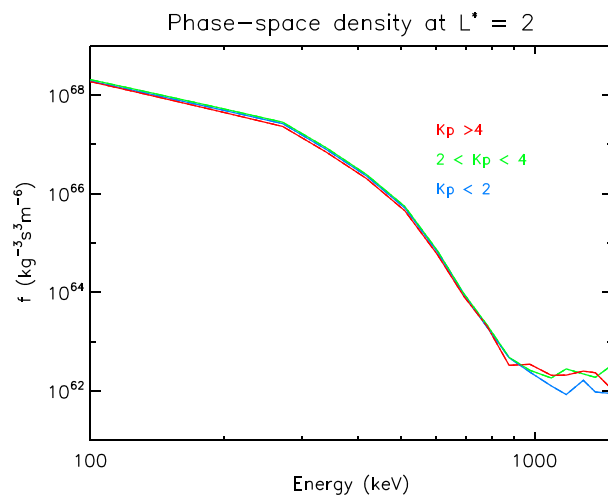


Figure 2. The electron phase-space density ($\text{kg}^{-3} \text{s}^3 \text{m}^{-6}$) for $J = 0 \text{ m T}^{\frac{1}{2}}$ and a range of energies at $L^* = 2$ for (blue) $Kp < 2$, (green) $2 \leq Kp \leq 4$, and (red) $Kp > 4$.

very little gradient in the phase-space density. Finally, *Turner et al.* [2012c] reported observations of constant phase-space density for $6.1 \leq L^* \leq 8.5$ at constant first and second invariant for $\mu = 200 \text{ MeV/G}$. Based on this, we have adopted a phase-space density profile in L^* on the minimum-energy boundary, $\mu_{\text{min}} = 100 \text{ MeV/G}$ that is constant for $L^* > 5.5$. This assumption will be discussed further in sections 6 and 7.

To calculate the phase-space density on the low-energy boundary for $L^* \leq 5.5$, we first averaged the CRRES phase-space density for $\mu = 100 \text{ MeV/G}$ (from before 24 March 1991) for $2 \leq Kp \leq 4$ for each L^* in the range $2 \leq L^* \leq 5.5$. The resulting radial profile is shown in Figure 3. For the reasons outlined above, we assume that the phase-space density is constant at $\mu = \mu_{\text{min}}$ for $L^* > 5.5$. The averaged radial profile is then scaled up and down according to the value chosen for the phase-space density for $L^* > 5.5$, to provide a time-dependent phase-space density on the low-energy boundary.

To prescribe the phase-space density for $L^* > 5.5$, we use a model that was recently presented for the outer boundary condition for diffusion models [*Shin and Lee, 2013*]. The *Shin and Lee* model averages data from the THEMIS spacecraft between 7 and $8 R_E$ on the nightside to derive a solar wind-driven model for the electron flux for energies between 31 and 719 keV. We assume that the model provides the flux at $7.5 R_E$ on the

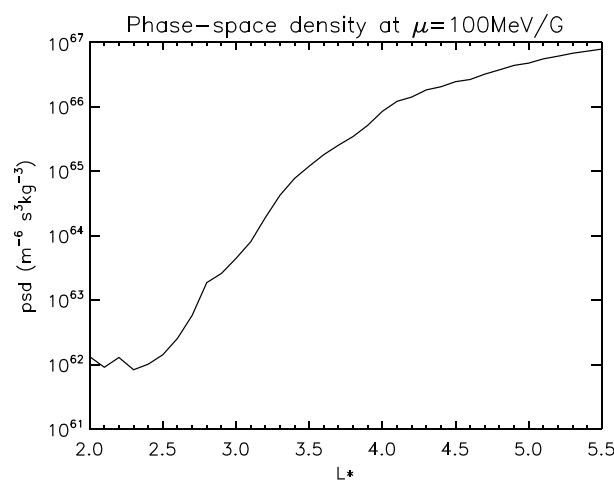


Figure 3. The electron phase-space density profile ($\text{kg}^{-3} \text{s}^3 \text{m}^{-6}$) for $\mu = 100 \text{ MeV/G}$ and $J = 0 \text{ m T}^{\frac{1}{2}}$ used to define the low-energy boundary condition.

Brautigam and Albert [2000] show radial profiles of the phase-space density for different values of μ at two different times during the CRRES mission. For $\mu = 100 \text{ MeV/G}$, the profiles have little gradient for $L^* > 5$, whereas for $\mu = 1000 \text{ MeV/G}$, they have a definite negative gradient at $L^* = 6$. *Iles et al. [2006]* also considered radial profiles for CRRES data at different values of μ . For the lowest value of μ they considered (150 MeV/G), they described the phase-space density as having a characteristic shape; “a steep positive gradient at low L^* up to a transition value, and then the phase-space density is relatively flat for L^* greater than the transition value or has a small positive gradient.” *Chen et al. [2005]* examined phase-space density gradients between $6.3 \leq L^* \leq 6.8$. At their lowest $\mu = 167 \text{ MeV/G}$, there is again

very little gradient in the phase-space density. Finally, *Turner et al.* [2012c] reported observations of constant phase-space density for $6.1 \leq L^* \leq 8.5$ at constant first and second invariant for $\mu = 200 \text{ MeV/G}$. Based on this, we have adopted a phase-space density profile in L^* on the minimum-energy boundary, $\mu_{\text{min}} = 100 \text{ MeV/G}$ that is constant for $L^* > 5.5$. This assumption will be discussed further in sections 6 and 7.

To calculate the phase-space density on the low-energy boundary for $L^* \leq 5.5$, we first averaged the CRRES phase-space density for $\mu = 100 \text{ MeV/G}$ (from before 24 March 1991) for $2 \leq Kp \leq 4$ for each L^* in the range $2 \leq L^* \leq 5.5$. The resulting radial profile is shown in Figure 3. For the reasons outlined above, we assume that the phase-space density is constant at $\mu = \mu_{\text{min}}$ for $L^* > 5.5$. The averaged radial profile is then scaled up and down according to the value chosen for the phase-space density for $L^* > 5.5$, to provide a time-dependent phase-space density on the low-energy boundary.

To prescribe the phase-space density for $L^* > 5.5$, we use a model that was recently presented for the outer boundary condition for diffusion models [*Shin and Lee, 2013*]. The *Shin and Lee* model averages data from the THEMIS spacecraft between 7 and $8 R_E$ on the nightside to derive a solar wind-driven model for the electron flux for energies between 31 and 719 keV. We assume that the model provides the flux at $7.5 R_E$ on the equator. For a given Kp , the L^* corresponding to $7.5 R_E$ on the equator are calculated for MLTs on the nightside using the *Tsyganenko '89* magnetic field model [*Tsyganenko, 1989*]. These nightside L^* values are then averaged over MLT to give a Kp -dependent L^* for the location of the flux given by the *Shin and Lee* model.

The energy equivalent to μ_{min} is calculated for a 90° equatorial pitch angle at this L^* , assuming a dipole field. The *Shin and Lee* model is then used to determine the flux at this energy. The flux is then converted to phase-space density. Other equatorial pitch angles are determined using a $\sin \alpha$ dependence.

This gives the equatorially mirroring phase-space density at μ_{min} for an L^* in the range $5.4 \leq L^* \leq 7.5$. To define

the phase-space density on μ_{\min} for the entire L^* range we assume the phase-space density is constant for $L^* > 5.5$ and scale the averaged radial profile in Figure 3 so that the phase-space density at $L^* > 5.5$ is equal to the value derived from the Shin and Lee model. This approach will be discussed further in sections 6 and 7.

This method of calculating the phase-space density on the low-energy boundary produces a time-dependent phase-space density that depends on Kp and the solar wind speed. The model runs described in section 3 are under constant conditions and require a fixed value of the phase-space density on the low-energy boundary. To determine this fixed value of the phase-space density, we calculated the phase-space density for $\mu_{\min} = 100$ MeV/G for the whole of the period 1990–1991 using the model for the low-energy boundary condition described above. We then selected the lowest value of the phase-space density calculated for this period as the phase-space density for the model runs in section 3.

3. Creation of the Outer Radiation Belt

In the model described above, the only source for the outer radiation belt is the electron source on the low-energy boundary, which corresponds to a very soft electron energy spectrum. This spectrum represents low-energy electrons (around tens of keV at larger L^*) from the plasma sheet that are transported toward the Earth due to convection electric fields. These electrons may be accelerated by interaction with chorus waves to form the outer radiation belt at energies of several MeV, unless losses or other transport processes dominate. In this section we investigate whether an outer belt can be formed in our model, where it would be located, and whether it would resemble observations.

Figure 4 shows that the acceleration due to chorus waves is sufficient to create the outer belt from our low-energy source. At the start of the simulation the radiation belts are completely empty. The only sources are on the minimum-energy boundary and the minimum L^* boundary. Kp is kept constant at $Kp = 2$, and the phase-space density on the low-energy boundary is set at the lowest value computed for the period 1990–1991 using the low-energy boundary model described above, to represent difficult conditions under which to form the belt. For 700 keV electrons, model results are omitted for $L^* < 2.9$ as the lowest energy of the computational grid exceeds 700 keV for 90° electrons at these L^* . For similar reasons for the 1500 keV electrons, no model results are shown for $L^* < 2.1$.

Under these conditions, it only takes about a day for a “belt” to be visible in the 700 keV electrons (Figure 4, bottom), when the electron flux exceeds $0.01 \text{ cm}^{-2} \text{ s}^{-1} \text{ sr}^{-1} \text{ keV}^{-1}$. After about 20 days these electrons appear to reach a steady state. The 1.5 MeV electrons (Figure 4, middle) appear about a day after the 700 keV electrons but take much longer (about 30 days) to approach a steady state. The 3 MeV electrons (Figure 4, top) take even longer to appear and have not reached a steady state after 30 days. Since there is no energy dependence in the radial diffusion coefficients, this delay is due to the time taken to accelerate electrons to higher energies by chorus.

Figure 5 shows (left) radial profiles of the flux after 30 days at the same energies as Figure 4 and (right) phase-space density at fixed values of the first and second invariants. In the top two panels, where $Kp = 2$, the location of the peaks in the flux move inward as the energy increases, from near the plasmopause ($L^* \approx 5.0$) at 700 keV to $L^* \approx 4.0$ at 3 MeV. This agrees well with observations of the average quiet time flux [e.g., Walt, 1994]. The phase-space density peaks near the plasmopause, and the phase-space density profiles also agree generally with observations, having a steeper gradient on the earthward side of the peak [see Turner *et al.*, 2012c]. The earthward movement of the peaks in the flux with energy can be explained by as a combination of the energy-dependent conversion from flux to phase-space density, $J = p^2 f$, and the action of plasmaspheric hiss. In the absence of hiss (not shown here), the peaks show a less pronounced earthward trend with energy; since hiss is only included within the plasmopause, including hiss in the simulation reduces the flux on the earthward side of the peak, moving the peak to higher L^* . As hiss is strongest at energies around 400 keV [Glauert *et al.*, 2014] and decreases with increasing energy, hiss erodes the earthward side of the peak more for the lower energies, increasing the range of L^* over which the peaks occur.

Figure 5 (bottom) shows the radial profiles for $Kp = 4$. The peaks in both the phase-space density and the flux move to lower L^* compared to those for $Kp = 2$, as a result of the inward motion of the plasmopause, consistent with Shprits *et al.* [2012]. The gradients also become steeper. For $L^* > 5$ with $Kp = 4$, although

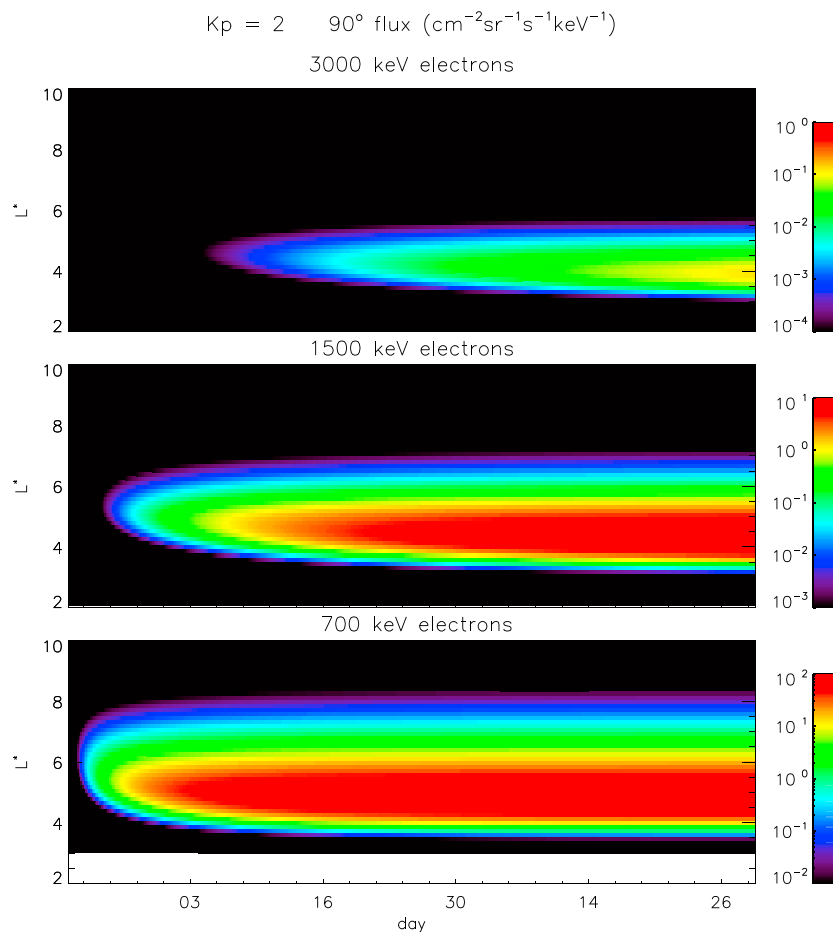


Figure 4. The 90° electron flux ($\text{cm}^{-2} \text{s}^{-1} \text{sr}^{-1} \text{keV}^{-1}$) for 30 days with $Kp = 2$, starting with an empty outer radiation belt, for (top) 3 MeV electrons, (middle) 1.5 MeV electrons, and (bottom) 700 keV electrons.

the wave acceleration is increased relative to $Kp = 2$, radial diffusion proportionally increases the outward transport more, leading to the noticeably steeper gradient in the phase-space density at larger L^* .

The flux of 700 keV electrons is often observed to exceed $10^4 \text{ cm}^{-2} \text{ s}^{-1} \text{sr}^{-1} \text{keV}^{-1}$ (see Figure 6) which is much higher than the peak flux ($\sim 100 \text{ cm}^{-2} \text{ s}^{-1} \text{sr}^{-1} \text{keV}^{-1}$) in Figure 4. However, Figure 6 assumed a constant $Kp = 2$ and a low value for the phase-space density on the low-energy boundary. In more active conditions there will be more acceleration due to chorus waves and the phase-space density on the low-energy boundary will increase, resulting in much higher peak flux values.

The model demonstrates that an outer radiation belt can be formed by wave acceleration from a very soft spectrum, without inward radial diffusion from a source in the outer magnetosphere.

4. Comparison With Data

In the previous section we demonstrated that the model can reproduce some general features of the outer radiation belt. To investigate whether the model can reproduce observations, we simulate a period from the CRRES mission.

4.1. CRRES Data

In this study, radiation belt data recorded by the MEA (Medium Electrons A) experiment on the CRRES spacecraft [Johnson and Kierein, 1992] were used. The data processing is described in Vampola et al. [1992]. The adiabatic invariants L^* and $K = J/2\sqrt{2m_e\mu}$ were calculated as a function of half orbit, local pitch angle in steps of 5° and McIlwain L in steps of 0.1 L . The invariants L^* and K were computed using the ONERA DESP library v4.2 [Boscher et al., 2008] with the International Geomagnetic Reference Field model at the middle of

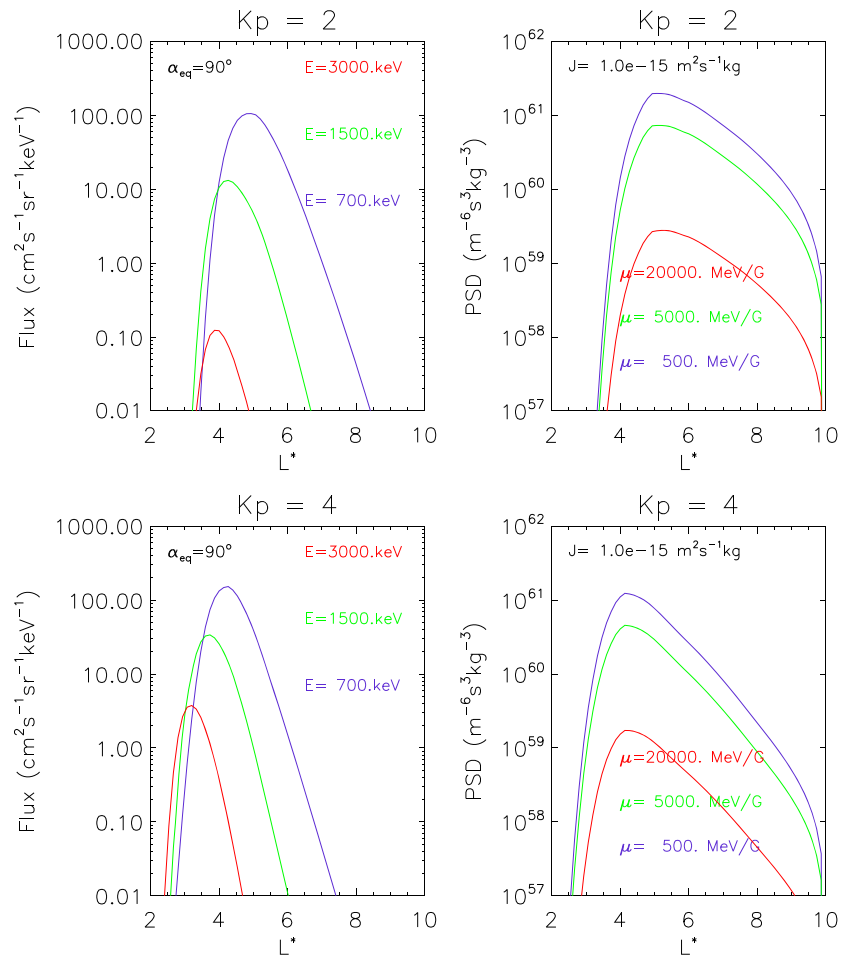


Figure 5. (left) The 90° electron flux ($\text{cm}^{-2} \text{s}^{-1} \text{sr}^{-1} \text{keV}^{-1}$) and (right) phase-space density at steady state for (top) $Kp = 2$ and (bottom) $Kp = 4$.

the appropriate year and the Tsyganenko '89 external magnetic field model [Tsyganenko, 1989]. The equatorial pitch angle (α) was determined as a function of half orbit, local pitch angle, and McIlwain L using the relation $Y/\sin \alpha = K/(L^* R_E \sqrt{B_{\text{eq}}})$, where B_{eq} is the (model) equatorial magnetic field strength and Y is given by

$$Y(y) = 2y \int_y^1 u^{-2} T(u) du \tag{9}$$

where $y = \sin \alpha$ and $T(y)$ is related to the bounce period, τ_B , by $T(y) = \tau_B p / (4 m L R_E)$ [Schulz and Lanzerotti, 1974]. Finally, the data were interpolated onto a regular grid in half orbit, equatorial pitch angle in steps of 5° and L^* , in steps of 0.1 R_E .

4.2. Results

In Figure 6 we compare the model results with observations for a 7 day period starting on 26 August 1991 (day 238) using data from the CRRES mission. Hourly averaged solar wind data, from the IMP8 (Interplanetary Monitoring Platform 8) spacecraft, is intermittent during the CRRES mission but the coverage during this period is reasonable (Figure 6e). As indicated by Kp (Figure 6f), the first day and a half of this period are relatively quiet, until a storm occurs around 17:00 UT on 27 August (day 239), associated with a modest increase in the solar wind velocity (Figure 6e) and a rise in Kp . The solar wind velocity increases again on day 242. Both these increases in the solar wind velocity are associated with flux dropouts that penetrate to about $L^* = 3.5$ for both 782 (Figure 6c) and 1090 (Figure 6a) keV electrons.

Figure 6 compares the model results (6b and 6d) and CRRES data (6a and 6c) for energies of 782 (6c and 6d) and 1090 (6a and 6b) keV with an equatorial pitch angle of 87.5°. The model uses the CRRES data for mid-night on 25 August to supply the initial condition, but no CRRES data are used for the boundary conditions.

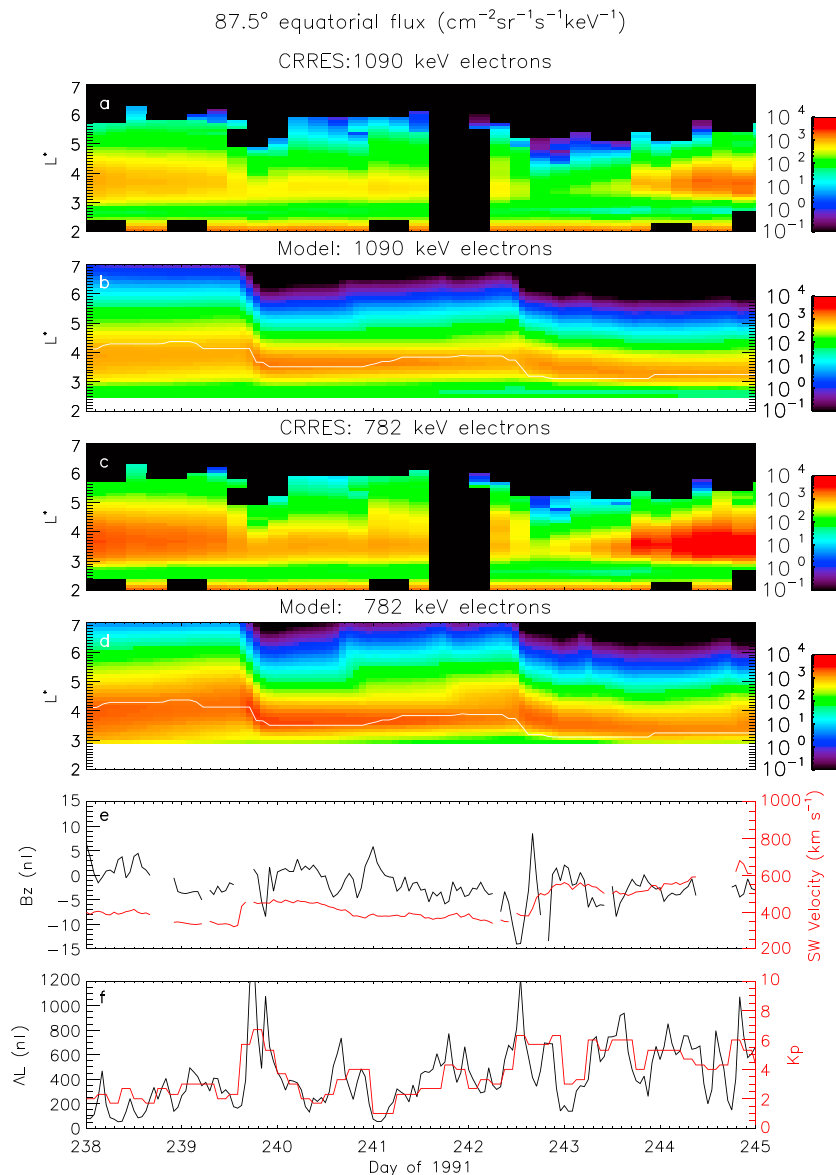


Figure 6. The 87.5° electron flux ($\text{cm}^{-2}\text{s}^{-1}\text{sr}^{-1}\text{keV}^{-1}$) for 26 August to 2 September 1991. (a) Observations from the CRRES spacecraft for 1090 keV electrons. (b) Model results for 1090 keV electrons. (c) Observations from the CRRES spacecraft for 782 keV electrons. (d) Model results for 782 keV electrons. (e) IMF B_z (nT) and solar wind velocity (km/s). (f) AE and K_p indices.

During both storms, the model shows a flux dropout that penetrates to about $L^* = 4$, though the dropout is not as pronounced as in the data at the lower L^* . In the model, this dropout is primarily due to the increased outward radial diffusion as a consequence of the increase in K_p during the storm, though there may be increased precipitation as well. After the second storm, the data show a recovery of the flux over the next 2 days to above prestorm levels for $L^* > 3$. There is a small increase in the model flux around $L^* = 5$ following the storm, but the model does not show the same sort of recovery as the data. The reasons for this will be discussed in section 7.

5. Modeling the Last Closed Drift Shell

The simulations shown in Figures 4 and 6 assume a fixed outer boundary at $L^* = 10$, where the phase-space density is set to zero. This equates to assuming that the LCDS is at $L^* = 10$. In reality the location of the LCDS will be constantly changing. This could be modeled with a moving outer boundary, but in a

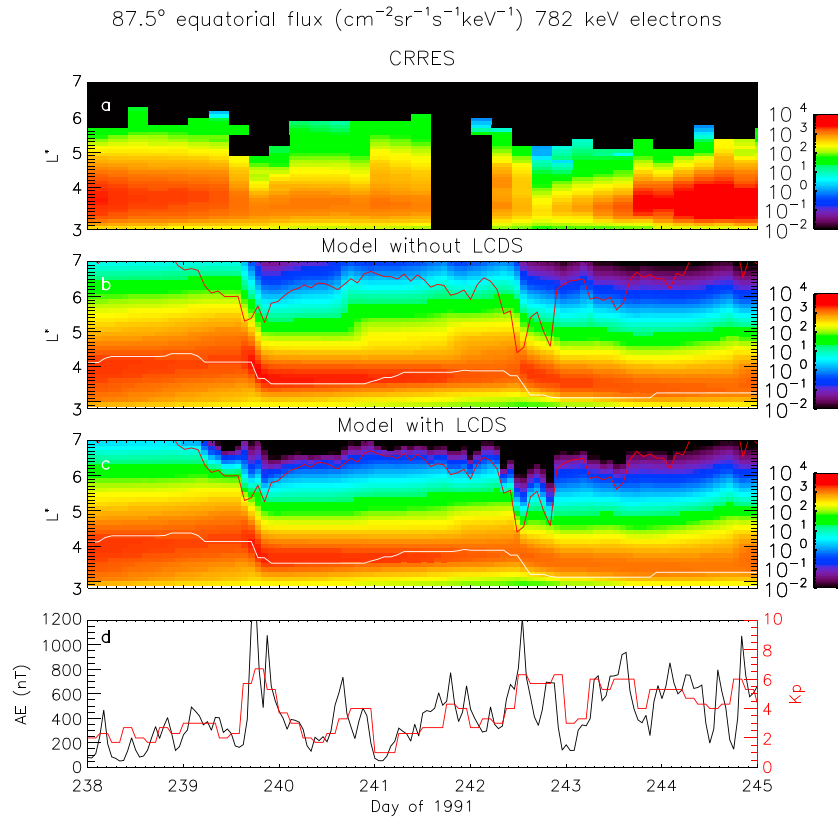


Figure 7. The 87.5° electron flux ($\text{cm}^{-2} \text{s}^{-1} \text{sr}^{-1} \text{keV}^{-1}$) for 782 keV electrons for 26 August to 2 September 1991. (a) Observations from the CRRES spacecraft. (b) Model results without LCDS; white line shows plasmopause location, and red line shows LCDS for $\alpha = 90^\circ$. (c) Model results with LCDS. (d) AE and Kp indices.

three-dimensional model, this can be cumbersome. An alternative approach is to model the location of the LCDS and then apply a loss term between the LCDS and the outer boundary [Su et al., 2010; Yu et al., 2013; Shprits et al., 2013]. This approach is also adopted here.

The Shue model [Shue et al., 1998] is widely used to model the location of the magnetopause as a function of solar wind parameters. However, Case and Wild [2013] demonstrated that it tends to overestimate the magnetopause standoff distance by about $1 R_E$. Matsumura et al. [2011] used test particle simulations to quantify the relationship between the magnetopause location and the LCDS for two different pitch angles. Based on their Figure 4, we have adopted the model

$$L_{\text{LCDS}}^*(\alpha) = (L_m - 1)(1.6375 - .00975\alpha) + 0.05387\alpha - 4.8937 \quad (10)$$

where L_m is the magnetopause standoff distance from the Shue model in R_E and $L_{\text{LCDS}}^*(\alpha)$ is the LCDS for an equatorial pitch angle α , measured in degrees. An extra loss term of the form $-f/\tau_{\text{mp}}$ is added to equation (1), where τ_{mp} is set to half the drift period if $L^* > L_{\text{LCDS}}^*$ and τ_{mp} is infinite otherwise.

Figure 7 shows the same period as Figure 6 for near-equatorially mirroring 782 keV electrons. Figure 7a shows the CRRES data. Figure 7b reproduces the results shown in Figure 6d. Finally, Figure 7c shows the result when the location of the LCDS is included in the model. The white lines show the location of the LCDS for 90° electrons when this is inside $L^* = 7$ and the red lines show the location of the plasmopause. Note that the color scale in Figure 7 has been changed from that in 6 to emphasize the results. Inside of $L^* = 6$, there is very little difference between the two simulations. This is because our outer boundary condition ($f = 0$) means there is always an outward gradient in phase-space density and the introduction of losses outside the LCDS only increases the gradient inside $L^* = 6$ slightly.

Yu et al. [2013] modeled the location of the LCDS in a 1-D radial diffusion model with losses due to wave-particle interactions and concluded that magnetopause shadowing could account for losses outside

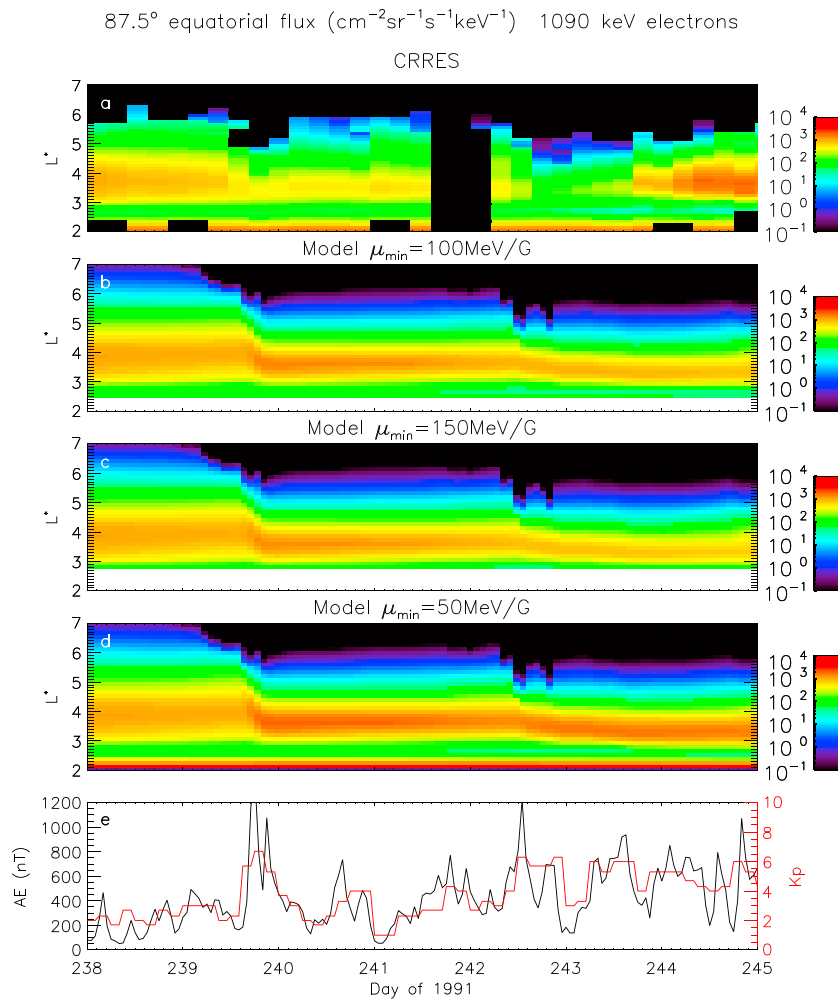


Figure 8. The 87.5° electron flux ($\text{cm}^{-2} \text{s}^{-1} \text{sr}^{-1} \text{keV}^{-1}$) for 1090 keV electrons for 26 August to 2 September 1991. (a) Observations from the CRRES spacecraft. (b) Model results with $\mu_{\text{min}} = 100 \text{ MeV/G}$. (c) Model results with $\mu_{\text{min}} = 150 \text{ MeV/G}$. (d) Model results with $\mu_{\text{min}} = 50 \text{ MeV/G}$. (e) AE and Kp indices.

of $L^* = 5$ but that another process may contribute to losses inside of $L^* = 5$. It is possible that the radial diffusion model used here (and by Yu et al.) may underestimate the radial diffusion during these active periods [Zhao and Li, 2013]. If the radial diffusion is underestimated, then the extra diffusion would increase losses and extend them to lower L^* .

Alternatively, the losses due to plasmaspheric hiss in our model are only included inside the plasmasphere, the location of which is determined by the O'Brien and Moldwin model and shown by the white line in Figure 7b. During both dropouts this lies inside $L^* = 3.5$. If the plasmopause was actually further out in L^* , then plasmaspheric hiss would extend further out in L^* , the peak flux would be reduced, and the dropout would be enhanced. Finally, there may be additional losses from other types of wave (e.g., EMIC waves and hiss in plumes) that are not included in our model.

Our simulation results show that even though the LCDS may have come to $L^* = 5.5$, it has little influence on the flux dropout, since there is always outward radial diffusion in our model. However, this may not be true for larger events.

6. Location of the Minimum-Energy Boundary

At low (10 keV) energies, convection processes dominate the behavior of the electrons and the phase-space density usually has a positive gradient at larger L^* as more electrons are injected into the magnetosphere from the tail at larger L^* . At high energies, diffusion is the dominant process and the gradient is negative at

larger L^* as electrons diffuse out to the magnetopause. Our low-energy boundary condition assumes that between these two regimes, there is a value of μ where the phase-space density gradient (at constant first and second invariant) is zero for $L^* > 5.5$.

In the results presented so far, we have placed the low-energy boundary at $\mu_{\min} = 100$ MeV/G for equatorially mirroring electrons. Figure 8 illustrates the effect of varying the value of μ_{\min} . Figure 8a shows the data from the CRRES spacecraft. Figure 8d shows the same simulation as Figure 7 but with $\mu_{\min} = 50$ MeV/G. The flux is overpredicted compared to the data, probably because at the lower energies convection due to the electric and magnetic fields should be included in the model. Figure 8c shows the result when $\mu_{\min} = 150$ MeV/G. Now the flux is underpredicted, particularly later in the simulation (days 243–245). Figure 8b reproduces the flux when $\mu_{\min} = 100$ MeV/G for comparison and provides the best agreement with the observations.

This value of $\mu_{\min} = 100$ MeV/G is consistent with the results in *Brautigam and Albert* [2000] but lower than that observed by *Turner et al.* [2012c]. The results in Turner et al. represent one set of observations taken during disturbed conditions. The radial profiles in *Brautigam and Albert* [2000] suggest that a lower value (100 MeV/G) may be more appropriate. If there is a value of μ where $\partial f / \partial L^*$ is near zero, it may depend on the level of geomagnetic activity, solar wind conditions, the level of substorm activity, and other factors. Since we use one value of μ_{\min} for all conditions, then it must represent an average value for all conditions. More observations of the phase-space density are needed to investigate this further.

7. Discussion

We have shown that in our model, an outer radiation belt can be created from a low-energy source alone; it does not require a source at the outer boundary. Low-energy electrons in the outer region are accelerated by interaction with the chorus waves over a large region of space from the plasmopause out to $L^* = 10$. At larger L^* radial transport is rapid and dominates the net acceleration (i.e., the acceleration taking losses due to pitch angle scattering into account) and electrons are transported to the outer boundary. Around $L^* = 4$ – 5 acceleration exceeds transport and the outer belt peaks. Inside the plasmopause, the absence of chorus means that transport and loss are the dominant processes, producing the inner edge of the outer belt.

We have modeled the outer radiation belt using a three-dimensional model by placing the outer boundary at $L_{\max}^* = 10$ and setting the phase-space density to zero here, representing losses to the magnetopause. This approach is possible because we have new chorus diffusion coefficients for the region $1.5 \leq L^* \leq 10$. The choice of $L_{\max}^* = 10$ as the outer boundary was determined by the extent of the chorus diffusion matrix, but the results are not very sensitive to the choice of L_{\max}^* , provided that L_{\max}^* is not too close to the outer belt, typically $L_{\max}^* > 8.5$. Simulations (not shown here) using $L_{\max}^* = 9$ are indistinguishable from those with $L_{\max}^* = 10$. In this outer region, radial diffusion is very rapid, since the Brautigam and Albert diffusion coefficients are proportional to $(L^*)^{10}$, so the precise location of the boundary has little effect on the final solution, provided it is placed at $L^* > 8.5$. Although the Brautigam and Albert diffusion coefficients were derived using data at $L^* = 4$ and $L^* = 6.6$, we are using them for $2 \leq L^* \leq 10$ since no suitable radial diffusion coefficients have been published for $6.6 \leq L^* \leq 10$. However, as noted above, the timescale for radial diffusion in this region is very rapid and having a very accurate determination of the diffusion coefficient may not make an appreciable difference to the solution, though measurements to confirm that they are large are required.

As illustrated in Figure 1, acceleration due to chorus waves is very rapid at large values of L^* [*Horne et al.*, 2013b]. Significant electron acceleration occurs outside of $L^* = 7$, although the peak in phase-space density often lies inside $L^* = 6$. This may explain much of the success of simple 1-D radial diffusion models for the outer radiation belt [e.g., *Lam et al.*, 2007; *Ozeke et al.*, 2012]. Although these models do not explicitly include the acceleration due to wave-particle interactions, they are introducing it implicitly through their outer boundary condition; the phase-space density on the outer boundary is set using data from a location where there is already significant acceleration due to wave-particle interactions. The models then transport this already accelerated electron population to lower L^* .

ULF wave power correlates with solar wind speed and is significantly enhanced when the solar wind exceeds 500 km s^{-1} [*Engebretson et al.*, 1998]. Since flux dropout events are associated with an increase in the solar wind dynamic pressure [*Ohtani et al.*, 2009], this suggests that they should also be associated with

increased ULF wave power. The Brautigam and Albert radial diffusion coefficients use the Kp index as a proxy for the ULF wave power. Since increased Kp is not necessarily associated with increased solar wind speed or dynamic pressure, the Brautigam and Albert diffusion coefficients may underestimate the radial transport when the magnetopause is compressed. An increase in the radial diffusion, above the current Kp -determined value, when the magnetopause moves closer to the Earth would enhance the flux dropouts in the model, possibly extending them to lower L^* . An investigation of radial diffusion during magnetopause compressions would prove illuminating.

The model is unable to capture the full extent of the acceleration following the second storm on day 242. Our chorus model, driven by Kp [Horne *et al.*, 2013b], has five activity bands, the most active of which is $Kp > 4$. This limitation is due to a lack of data to fully define the chorus model during very active periods. For most of the period following the second storm, $Kp > 4$ and $Kp = 6$ for extended periods. As a result, chorus acceleration will be significantly underestimated in the model during this period. Further work is required to improve the chorus model during very active conditions.

In order to provide a low-energy boundary condition for $2 \leq L^* \leq 10$ that is independent of data, we have placed the boundary at $\mu_{\min} = 100$ MeV/G, assumed the phase-space density is constant for $L^* > 5.5$, and used a statistical model to determine the constant value. The combination of these assumptions places limitations on the current model. Our choice of $\mu_{\min} = 100$ MeV/G is higher than other authors. Varotsou *et al.* [2008] use a constant phase-space density for all L^* at $\mu_{\min} = 0.1$ MeV/G, a value of μ_{\min} where convection effects that are omitted from the model are likely to be significant. Subbotin and Shprits' [2009] choice of $\mu_{\min} = 11$ MeV/G is more realistic for models that omit convection, but their assumption that the phase-space density is constant in time is unlikely to be a good approximation at times, for example, during injection events. However, in models that specify the phase-space density on outer L^* boundary, the outer L^* boundary condition may at least partly compensate for inaccuracies in the low-energy boundary by providing a realistic energy spectrum that can be transported inward.

In our model, changes in the low-energy electron population, for example, injections during substorms, can only be incorporated via the low-energy boundary condition. Since we assume a constant phase-space density for $L^* > 5.5$ and drive this boundary using a statistical model we are unlikely to completely capture the dynamics associated with individual events. For example, during the storm on day 242 there is a large increase in the AE index, which is likely to be associated with an injection of low-energy electrons during a substorm. Although the phase-space density on our low-energy boundary will change, the statistical model may not capture the actual increase accurately. Combined with the limitations of the chorus model for $Kp > 4$ discussed earlier, this may contribute to the inability of the model to reproduce the increase in flux following the second storm.

To derive the low-energy boundary condition, the current model assumes that there is a value of μ where the phase-space density is constant with L^* for $L^* > 5.5$ and has a fixed, scalable profile at lower L^* . This clearly simplifies the modeling since it means that if the phase-space density is known at one value of L^* , it can be determined for all L^* . The evidence for a flat phase-space density beyond $L^* = 5.5$ is discussed in section 2.3. The use of a fixed radial profile in the slot region may not be very accurate as this region can fill during very active conditions. However, in this region there is little or no acceleration due to chorus waves and radial diffusion is weaker than at larger L^* , so the low-energy boundary condition has little effect on the flux at MeV energies here. Improvements to the low-energy boundary condition are the subject of ongoing work.

On the L_{\min} and E_{\min} boundaries we determine the 90° equatorial flux and then assume a $\sin \alpha$ pitch angle dependence for other equatorial pitch angles. This approach has been used by many previous authors [e.g., Albert and Young, 2005; Subbotin and Shprits, 2009; Woodfield *et al.*, 2014]. Glauert *et al.* [2014] fitted $\sin^n \alpha$ distributions to the CRRES data and typically found that $0.05 < n < 0.5$. Rerunning our simulations using $\sin^{0.05} \alpha$ distributions instead of $\sin \alpha$ shows that changing the pitch angle dependence of the boundary condition in this way has very little effect on the results for electrons with an equatorial pitch angle close to 90° .

We have described a simple method for taking the location of the LCDS into account in three-dimensional radiation belt models. For the test case presented here, including the LCDS in the model with a zero outer boundary did not have a dramatic effect. However, the magnetopause only came in to about $7 R_E$ in this

example. Unfortunately, there is limited coverage of solar wind data for the CRRES period, limiting the number of dropout events that can be studied from this period. Further work is planned to use Van Allen Probes data to validate and improve the model now that pitch angle-resolved data are available.

The model for the LCDS includes the effect of drift shell splitting but is based on a few results at only two pitch angles. Further investigation of the behavior of the LCDS under different conditions could improve the model. In particular, more test particle simulations could be used to determine a better relationship between the LCDS and the magnetopause location; magnetic field models could be used directly (as in the one-dimensional study of *Yu et al.* [2013]) to determine the location of the LCDS or indirectly by developing a relationship between the LCDS and solar wind parameters and geomagnetic indices.

Chorus waves, plasmaspheric hiss, and LGW have been included in the model, with the plasmaspheric hiss being confined to the plasmasphere. Hiss in plumes is not included here but may contribute to losses in the outer belt [*Summers et al.*, 2008]. Other waves such as magnetosonic waves and electromagnetic ion cyclotron (EMIC) waves may also play a role in radiation belt dynamics. Magnetosonic waves can accelerate electrons between ~ 10 keV and a few MeV in the outer radiation belt on a timescale of 1–2 days for waves with intensities of the order 50,000 pT² [*Horne et al.*, 2007]. EMIC waves resonate with highly relativistic electrons [*Lyons and Thorne*, 1972; *Horne and Thorne*, 1998; *Summers et al.*, 1998; *Albert*, 2003] causing pitch angle scattering and loss to the atmosphere [*Thorne*, 1974; *Thorne and Andreoli*, 1980]. Under certain circumstances they are able to resonate with electrons with energies of the order of 1 MeV and may be strong enough to cause strong diffusion scattering [e.g., *Meredith et al.*, 2003b]. Further work needs to be undertaken to produce geomagnetic activity and location-dependent diffusion coefficients for these types of wave.

The simulations presented here use the K_p index to drive the wave-particle interactions. The BAS Radiation Belt Model can also drive these interactions using the AE index, and it has been shown that this gives better results [*Glauert et al.*, 2014]. Using AE rather than K_p might, in particular, improve the modeling of the flux increase following the second storm (day 242) as AE correlates better with substorm activity. However, the model described here was developed as part of a European Union FP7 project, SPACECAST (www.fp7-spacecast.eu) to develop forecasts for the radiation belts. At present, there are forecasts available for the K_p index [e.g., *Boberg et al.*, 2000] but not for the AE index so the K_p index has been employed here. The Shin and Lee model used for the low-energy boundary condition can be used for forecasting, even without a forecast of the solar wind velocity. It is driven by the maximum value of the solar wind velocity over an energy-dependent previous time period, which includes a time delay for energies > 65 keV. In quiet conditions, there is little variation in the solar wind velocity so the maximum solar wind velocity over the preceding hours is generally representative of the solar wind velocity over the next 3 h. In active conditions, the L^* used to determine the location for the Shin and Lee data is generally lower, the energy corresponding to $\mu_{\min} = 100$ MeV/G is higher, and typically, the time delay used in calculating the maximum value of the solar wind velocity is longer than the forecasting time (3 h). This allows the Shin and Lee model to be used for forecasting. However, the Shue model for the magnetopause location uses solar wind pressure and IMF B_z . A time delay (typically 1 h) can be assumed between measurements at the ACE spacecraft and changes to the magnetopause location but to forecast ahead of that requires a forecast of these parameters. Fortunately, as shown above, the model results inside geostationary orbit (typically around $L^* = 6$) are not very sensitive to the magnetopause model as, at present, an assumption of persistence is the only practical option for forecasting the measurements from ACE.

8. Summary and Conclusions

We have presented results from three-dimensional radiation belt simulations using a zero phase-space density at the outer boundary, representing losses to the magnetopause. The source of electrons in the simulation is the electron flux at the low-energy boundary, which is effectively a very soft spectrum and is assumed to arise from injection by convection electric fields.

Our principle conclusions are the following:

1. The existence and location of the outer radiation belt can be reproduced in our model without the need for a source at the outer boundary. Electrons at the low-energy boundary are accelerated by chorus waves to form the outer belt.

2. The increased radial diffusion that occurs during geomagnetically active conditions results in a depletion of the outer radiation belt that resembles a flux dropout event. With a zero phase-space density at the outer boundary, there is always an outward gradient in phase-space density. During active conditions this gradient increases; there is increased acceleration due to chorus waves, but increased radial diffusion dominates and results in more efficient transport to the outer boundary.
3. In the example studied here, modeling of flux dropout events is not greatly improved if additional losses are included outside the location of the LCDS. Since, in our model, there is always an outward gradient these additional losses only have a minor effect on the solution.
4. The choice of μ for the low-energy boundary is important for accurate simulations. A value of $\mu = 100$ MeV/G gives the best results in the simulations presented here but this requires further investigation.

Acknowledgments

This study is part of the British Antarctic Survey Polar Science for Planet Earth Programme. It was funded by The Natural Environment Research Council and the European Union Seventh Framework Programme (FP7/2007-2013) under grant agreement 262468. The data used to generate the plots in this paper are stored at the BAS Polar Data Centre and are available on request.

Michael Liemohn thanks Adam Kellerman and another reviewer for their assistance in evaluating this paper.

References

- Abel, B., and R. M. Thorne (1998a), Electron scattering loss in Earth's inner magnetosphere. 1. Dominant physical processes, *J. Geophys. Res.*, **103**, 2385–2396, doi:10.1029/97JA02919.
- Abel, B., and R. M. Thorne (1998b), Electron scattering loss in Earth's inner magnetosphere. 2. Sensitivity to model parameters, *J. Geophys. Res.*, **103**, 2397–2407, doi:10.1029/97JA02920.
- Albert, J. M. (2003), Evaluation of quasi-linear diffusion coefficients for EMIC waves in a multispecies plasma, *J. Geophys. Res.*, **108**(A6), 1249, doi:10.1029/2002JA009792.
- Albert, J. M. (2010), Diffusion by one wave and by many waves, *J. Geophys. Res.*, **115**, A00F05, doi:10.1029/2009JA014732.
- Albert, J. M., and S. L. Young (2005), Multidimensional quasi-linear diffusion of radiation belt electrons, *Geophys. Res. Lett.*, **32**, L14110, doi:10.1029/2005GL023191.
- Albert, J. M., N. P. Meredith, and R. B. Horne (2009), Three-dimensional diffusion simulation of outer radiation belt electrons during the October 9, 1990, magnetic storm, *J. Geophys. Res.*, **114**, A09214, doi:10.1029/2009JA014336.
- Baker, D. N. (2001), Satellite anomalies due to space storms, in *Space Storms and Space Weather Hazards*, edited by I. A. Daglis, p. 251, Springer, New York.
- Baker, D. N., J. B. Blake, R. W. Klebesadel, and P. R. Higbie (1986), Highly relativistic electrons in the Earth's outer magnetosphere: 1. Lifetimes and temporal history 1979–1984, *J. Geophys. Res.*, **91**(A4), 4265–4276, doi:10.1029/JA091iA04p04265.
- Baker, D. N., J. B. Blake, L. B. Callis, J. R. Cummings, D. Hovestadt, S. Kanekal, B. Klecker, R. A. Mewaldt, and R. D. Zwickl (1994), Relativistic electron acceleration and decay timescales in the inner and outer radiation belts: SAMPEX, *Geophys. Res. Lett.*, **21**(6), 409–412, doi:10.1029/93GL03532.
- Baker, D. N., et al. (1997), Recurrent geomagnetic storms and relativistic electron enhancements in the outer magnetosphere: ISTP coordinated measurements, *J. Geophys. Res.*, **102**(A7), 14,141–14,148, doi:10.1029/97JA00565.
- Beutier, T., and D. Boscher (1995), A three-dimensional analysis of the electron radiation belt by the *Salammô* code, *J. Geophys. Res.*, **100**, 14,853–14,861, doi:10.1029/94JA03066.
- Blake, J. B., W. A. Kolasinski, R. W. Fillius, and E. G. Mullen (1992), Injection of electrons and protons with energies of tens of MeV into L < 3 on 24 March 1991, *Geophys. Res. Lett.*, **19**(8), 821–824.
- Boberg, F., P. Wintoft, and H. Lundstedt (2000), Real time Kp predictions from solar wind data using neural networks, *Phys. Chem. Earth*, **25**(4), 275–280.
- Bortnik, J., and R. M. Thorne (2007), The dual role of ELF/VLF chorus waves in the acceleration and precipitation of radiation belt electrons, *J. Atmos. Sol. Terr. Phys.*, **69**, 378–386, doi:10.1016/j.jastp.2006.05.030.
- Bortnik, J., R. M. Thorne, T. P. O'Brien, J. C. Green, R. J. Strangeway, Y. Y. Shprits, and D. N. Baker (2006), Observation of two distinct, rapid loss mechanisms during the 20 November 2003 radiation belt dropout event, *J. Geophys. Res.*, **111**, A12216, doi:10.1029/2006JA011802.
- Boscher, D., S. Bourdarie, P. O'Brien, and T. Guild (2008), *ONERA-DESP library V4.2, Toulouse-France, 2004–2008*.
- Brautigam, D. H., and J. M. Albert (2000), Radial diffusion analysis of outer radiation belt electrons during the October 9, 1990, magnetic storm, *J. Geophys. Res.*, **105**, 291–309, doi:10.1029/1999JA000344.
- Case, N. A., and J. A. Wild (2013), The location of the Earth's magnetopause: A comparison of modeled position and in situ Cluster data, *J. Geophys. Res. Space Physics*, **118**, 6127–6135, doi:10.1002/jgra.50572.
- Chen, Y., R. H. W. Friedel, G. D. Reeves, T. G. Onsager, and M. F. Thomsen (2005), Multisatellite determination of the relativistic electron phase space density at geosynchronous orbit: Methodology and results during geomagnetically quiet times, *J. Geophys. Res.*, **110**, A10210, doi:10.1029/2004JA010895.
- Elkington, S. R. (2006), A review of ULF interactions with radiation belt electrons, in *Magnetospheric ULF Waves: Synthesis and New Directions*, vol. 169, edited by K. Takahashi et al., p. 177, AGU, Washington, D. C.
- Engebretson, M., K.-H. Glassmeier, M. Stellmacher, W. J. Hughes, and H. Lühr (1998), The dependence of high-latitude PcS wave power on solar wind velocity and on the phase of high-speed solar wind streams, **26**, 271–26,283, doi:10.1029/97JA03143.
- Falthammer, C.-G. (1965), Effects of time dependent electric fields on geomagnetically trapped radiation, *J. Geophys. Res.*, **70**, 2503–2516.
- Glauert, S. A., and R. B. Horne (2005), Calculation of pitch angle and energy diffusion coefficients with the PADIE code, *J. Geophys. Res.*, **110**, A04206, doi:10.1029/2004JA010851.
- Glauert, S. A., R. B. Horne, and N. P. Meredith (2014), Three-dimensional electron radiation belt simulations using the BAS radiation belt model with new diffusion models for chorus, plasmaspheric hiss, and lightning-generated whistlers, *J. Geophys. Res. Space Physics*, **119**, 268–289, doi:10.1002/2013JA019281.
- Horne, R. B., and R. M. Thorne (1998), Potential waves for relativistic electron scattering and stochastic acceleration during magnetic storms, *Geophys. Res. Lett.*, **25**, 3011–3014, doi:10.1029/98GL01002.
- Horne, R. B., S. A. Glauert, and R. M. Thorne (2003), Resonant diffusion of radiation belt electrons by whistler-mode chorus, *Geophys. Res. Lett.*, **30**(9), 1493, doi:10.1029/2003GL016963.
- Horne, R. B., et al. (2005a), Wave acceleration of electrons in the Van Allen radiation belts, *Nature*, **437**, 227–230, doi:10.1038/nature03939.
- Horne, R. B., R. M. Thorne, S. A. Glauert, J. M. Albert, N. P. Meredith, and R. R. Anderson (2005b), Timescale for radiation belt electron acceleration by whistler mode chorus waves, *J. Geophys. Res.*, **110**, A03225, doi:10.1029/2004JA010811.

- Horne, R. B., N. P. Meredith, S. A. Glauert, A. Varotsou, D. Boscher, R. M. Thorne, Y. Y. Shprits, and R. R. Anderson (2006), Mechanisms for the acceleration of radiation belt electrons, in *Recurrent Magnetic Storms: Corotating Solar Wind Streams*, *Geophys. Monogr. Ser.*, vol. 167, edited by B. Tsurutani et al., pp. 151–173, AGU, Washington, D. C.
- Horne, R. B., R. M. Thorne, S. A. Glauert, N. P. Meredith, D. Pokhotelov, and O. Santolík (2007), Electron acceleration in the Van Allen radiation belts by fast magnetosonic waves, *Geophys. Res. Lett.*, *34*, L17107, doi:10.1029/2007GL030267.
- Horne, R. B., S. A. Glauert, N. P. Meredith, D. Boscher, V. Maget, D. Heynderickx, and D. Pitchford (2013a), Space weather impacts on satellites and forecasting the Earth's electron radiation belts with SPACECAST, *Space Weather*, *11*, 169–186, doi:10.1002/swe.20023.
- Horne, R. B., T. Kersten, S. A. Glauert, N. P. Meredith, D. Boscher, A. Sicard-Piet, R. M. Thorne, and W. Li (2013b), A new diffusion matrix for whistler mode chorus waves, *J. Geophys. Res. Space Physics*, *118*, 6302–6318, doi:10.1002/jgra.50594.
- Hudson, M. K., S. R. Elkington, J. G. Lyon, C. C. Goodrich, and T. J. Rosenberg (1999), Simulation of radiation belt dynamics driven by solar wind variations, in *Sun-Earth Plasma Connections*, vol. 109, edited by J. L. Burch, R. L. Carovillano, and S. K. Antiochos, pp. 171–182, AGU, Washington, D. C.
- Iles, R. H. A., N. P. Meredith, A. N. Fazakerley, and R. B. Horne (2006), Phase space density analysis of the outer radiation belt energetic electron dynamics, *J. Geophys. Res.*, *111*, A03204, doi:10.1029/2005JA011206.
- Iucci, N., et al. (2005), Space weather conditions and spacecraft anomalies in different orbits, *Space Weather*, *3*, S01001, doi:10.1029/2003SW000056.
- Johnson, M. H., and J. Kierein (1992), Combined Release and Radiation Effects Satellite (CRRES), spacecraft and mission, *J. Spacecr. Rockets*, *29*, 556–563.
- Kennel, C. F., and H. E. Petschek (1966), Limit on stably trapped particle fluxes, *J. Geophys. Res.*, *71*(1), 1–28, doi:10.1029/JZ071i001p00001.
- Kim, K.-C., Y. Shprits, D. Subbotin, and B. Ni (2011a), Understanding the dynamic evolution of the relativistic electron slot region including radial and pitch angle diffusion, *Geophys. Res. Lett.*, *116*, A10214, doi:10.1029/2011JA016684.
- Kim, K.-C., D.-Y. Lee, Y. Shprits, H.-J. Kim, and E. Lee (2011b), Electron flux changes in the outer radiation belt by radial diffusion during the storm recovery phase in comparison with the fully adiabatic evolution, *J. Geophys. Res.*, *116*, A09229, doi:10.1029/2011JA016642.
- Lam, M. M., R. B. Horne, N. P. Meredith, and S. A. Glauert (2007), Modeling the effects of radial diffusion and plasmaspheric hiss on outer radiation belt electrons, *Geophys. Res. Lett.*, *34*, L20112, doi:10.1029/2007GL031598.
- Lenchek, A. M., S. F. Singer, and R. C. Wentworth (1961), Geomagnetically trapped electrons from cosmic ray albedo neutrons, *J. Geophys. Res.*, *66*(12), 4027–4046, doi:10.1029/JZ066i012p04027.
- Li, X., D. N. Baker, M. Temerin, T. E. Cayton, G. D. Reeves, R. A. Christensen, J. B. Blake, M. D. Looper, R. Nakamura, and S. G. Kanekal (1997), Multi-satellite observations of the outer zone electron variation during the November 3–4, 1993, magnetic storm, *J. Geophys. Res.*, *102*(A7), 14,123–14,140, doi:10.1029/97JA01101.
- Li, W., Y. Y. Shprits, and R. M. Thorne (2007), Dynamic evolution of energetic outer zone electrons due to wave-particle interactions during storms, *J. Geophys. Res.*, *112*, A10220, doi:10.1029/2007JA012368.
- Li, W., R. M. Thorne, V. Angelopoulos, J. Bortnik, C. M. Cully, B. Ni, O. LeContel, A. Roux, U. Auster, and W. Magnes (2009), Global distribution of whistler-mode chorus waves observed on the THEMIS spacecraft, *Geophys. Res. Lett.*, *36*, L09104, doi:10.1029/2009GL037595.
- Li, W., J. Bortnik, R. M. Thorne, and V. Angelopoulos (2011), Global distribution of wave amplitudes and wave normal angles of chorus waves using THEMIS wave observations, *J. Geophys. Res.*, *116*, A12205, doi:10.1029/2011JA017035.
- Lyons, L. R., and R. M. Thorne (1972), Parasitic pitch angle diffusion of radiation belt particles by ion cyclotron waves, *J. Geophys. Res.*, *77*, 5608–5616, doi:10.1029/JA077i028p05608.
- Lyons, L. R., and R. M. Thorne (1973), Equilibrium structure of radiation belt electrons, *J. Geophys. Res.*, *78*(13), 2142–2149, doi:10.1029/JA078i013p02142.
- Mathie, R. A., and I. R. Mann (2000), A correlation between extended intervals of ULF wave power and storm-time geosynchronous relativistic electron flux enhancements, *Geophys. Res. Lett.*, *27*, 3261–3264.
- Matsumura, C., Y. Miyoshi, K. Seki, S. Saito, V. Angelopoulos, and J. Koller (2011), Outer radiation belt boundary location relative to the magnetopause: Implications for magnetopause shadowing, *J. Geophys. Res.*, *116*, A06212, doi:10.1029/2011JA016575.
- Meredith, N. P., R. B. Horne, and R. R. Anderson (2001), Substorm dependence of chorus amplitudes: Implications for the acceleration of electrons to relativistic energies, *J. Geophys. Res.*, *106*, 13,165–13,178, doi:10.1029/2000JA900156.
- Meredith, N. P., R. B. Horne, D. Summers, R. M. Thorne, R. H. A. Iles, D. Heynderickx, and R. R. Anderson (2002), Evidence for acceleration of outer zone electrons to relativistic energies by whistler mode chorus, *Ann. Geophys.*, *20*, 967–979, doi:10.5194/angeo-20-967-2002.
- Meredith, N. P., R. B. Horne, R. M. Thorne, and R. R. Anderson (2003a), Favored regions for chorus-driven electron acceleration to relativistic energies in the Earth's outer radiation belt, *Geophys. Res. Lett.*, *30*(16), 1871, doi:10.1029/2003GL017698.
- Meredith, N. P., R. M. Thorne, R. B. Horne, D. Summers, B. J. Fraser, and R. R. Anderson (2003b), Statistical analysis of relativistic electron energies for cyclotron resonance with EMIC waves observed on CRRES, *J. Geophys. Res.*, *108*(A6), 1250, doi:10.1029/2002JA009700.
- Meredith, N. P., R. B. Horne, S. A. Glauert, R. M. Thorne, D. Summers, J. M. Albert, and R. R. Anderson (2006), Energetic outer zone electron loss timescales during low geomagnetic activity, *J. Geophys. Res.*, *111*, A05212, doi:10.1029/2005JA011206.
- Meredith, N. P., R. B. Horne, S. A. Glauert, and R. R. Anderson (2007), Slot region electron loss timescales due to plasmaspheric hiss and lightning generated whistlers, *J. Geophys. Res.*, *112*, A08214, doi:10.1029/2006JA012413.
- Meredith, N. P., R. B. Horne, S. A. Glauert, D. N. Baker, S. G. Kanekal, and J. M. Albert (2009), Relativistic electron loss timescales in the slot region, *J. Geophys. Res.*, *114*, A03222, doi:10.1029/2008JA013889.
- Meredith, N. P., R. B. Horne, A. Sicard-Piet, D. Boscher, K. H. Yearby, W. Li, and R. M. Thorne (2012), Global model of lower band and upper band chorus from multiple satellite observations, *J. Geophys. Res.*, *117*, A12209, doi:10.1029/2012JA017978.
- Miyoshi, Y., and R. Kataoka (2005), Ring current ions and radiation belt electrons during geomagnetic storms driven by coronal mass ejections and corotating interaction regions, *Geophys. Res. Lett.*, *32*, L21105, doi:10.1029/2005GL024590.
- Miyoshi, Y., A. Morioka, T. Obara, H. Misawa, T. Nagai, and Y. Kasahara (2003), Rebuilding process of the outer radiation belt during the 3 November 1993 magnetic storm: NOAA and Exos-D observations, *J. Geophys. Res.*, *108*(A1), 1004, doi:10.1029/2001JA007542.
- Miyoshi, Y. S., V. K. Jordanova, A. Morioka, M. F. Thomsen, G. D. Reeves, D. S. Evans, and J. C. Green (2006), Observations and modeling of energetic electron dynamics during the October 2001 storm, *J. Geophys. Res.*, *111*, A11502, doi:10.1029/2005JA011351.
- O'Brien, T. P., and M. B. Moldwin (2003), Empirical plasmopause models from magnetic indices, *Geophys. Res. Lett.*, *30*(4), 1152, doi:10.1029/2002GL016007.
- Ohtani, S., Y. Miyoshi, H. J. Singer, and J. M. Weygand (2009), On the loss of relativistic electrons at geosynchronous altitude: Its dependence on magnetic configurations and external configurations, *J. Geophys. Res.*, *114*, A01202, doi:10.1029/2008JA013391.
- Omura, Y., M. Hikishima, Y. Katoh, D. Summers, and S. Yagitani (2009), Nonlinear mechanisms of lower-band and upper-band VLF chorus emissions in the magnetosphere, *J. Geophys. Res.*, *114*, A07217, doi:10.1029/2009JA014206.

- Ozeke, L. G., I. R. Mann, K. R. Murphy, I. J. Rae, D. K. Milling, S. R. Elkington, A. A. Chan, and H. J. Singer (2012), ULF wave derived radiation belt radial diffusion coefficients, *J. Geophys. Res.*, *117*, A04222, doi:10.1029/2011JA017463.
- Paulikas, G. A., and J. B. Blake (1979), Effects of the solar wind on magnetospheric dynamics: Energetic electrons at synchronous orbit, in *Quantitative Modeling of Magnetospheric Processes, Geophys. Monogr. Ser.*, vol. 21, edited by W. P. Olsen, p. 180, AGU, Washington, D. C.
- Reeves, G. D., R. H. W. Friedel, R. D. Belian, M. M. Meier, M. G. Henderson, T. Onsager, H. J. Singer, D. N. Baker, X. Li, and J. B. Blake (1998), The relativistic electron response at geosynchronous orbit during the January 1997 magnetic storm, *J. Geophys. Res.*, *103*(A8), 17,559–17,570, doi:10.1029/97JA03236.
- Reeves, G. D., K. L. McAdams, R. H. W. Friedel, and T. P. O'Brien (2003), Acceleration and loss of relativistic electrons during geomagnetic storms, *Geophys. Res. Lett.*, *30*(10), 1529, doi:10.1029/2002GL016513.
- Roederer, J. G. (1970), *Dynamics of Geomagnetically Trapped Radiation*, Springer, New York.
- Saito, S., Y. Miyoshi, and K. Seki (2010), A split in the outer radiation belt by magnetopause shadowing: Test particle simulations, *J. Geophys. Res.*, *115*, A08210, doi:10.1029/2009JA014738.
- Santolik, O., C. A. Kletzing, W. S. Kurth, G. B. Hospodarsky, and S. R. Bounds (2014), Fine structure of large-amplitude chorus wave packets, *Geophys. Res. Lett.*, *41*, 293–299, doi:10.1002/2013GL058889.
- Schulz, M., and L. J. Lanzerotti (1974), *Particle Diffusion in the Radiation Belts*, Springer-Verlag, Berlin, Heidelberg, New York.
- Shprits, Y., M. Daae, and B. Ni (2012), Statistical analysis of phase space density buildups and dropouts, *J. Geophys. Res.*, *117*, A01219, doi:10.1029/2011JA016939.
- Shprits, Y. Y., R. M. Thorne, R. Friedel, G. D. Reeves, J. Fennell, D. N. Baker, and S. G. Kanekal (2006), Outward radial diffusion driven by losses at magnetopause, *J. Geophys. Res.*, *111*, A11214, doi:10.1029/2006JA011657.
- Shprits, Y. Y., D. Subbotin, A. Drozdov, M. E. Usanova, A. Kellerman, K. Orlova, D. N. Baker, D. L. Turner, and K.-C. Kim (2013), Unusual stable trapping of the ultrarelativistic electrons in the Van Allen radiation belts, *Nat. Phys.*, *9*, 699–703, doi:10.1038/nphys2760.
- Shue, J.-H., C. T. Russell, J. T. Steinberg, J. K. Chao, G. Zastenker, O. L. Vaisberg, S. Kokubun, H. J. Singer, T. R. Detman, and H. Kawano (1998), Magnetopause location under extreme solar wind conditions, *J. Geophys. Res.*, *103*(A8), 17,691–17,700, doi:10.1029/98JA01103.
- Shin, D.-K., and D.-Y. Lee (2013), Determining radial boundary conditions of outer radiation belt electrons using THEMIS observations, *J. Geophys. Res. Space Physics*, *118*, 2888–2896, doi:10.1002/jgra.50334.
- Su, Z., F. Xiao, H. Zheng, and S. Wang (2010), STEERB: A three-dimensional code for storm-time evolution of electron radiation belt, *J. Geophys. Res.*, *115*, A09208, doi:10.1029/2009JA015210.
- Su, Z., F. Xiao, H. Zheng, and S. Wang (2011), CRRES observation and STEERB simulation of the 9 October 1990 electron radiation belt dropout event, *Geophys. Res. Lett.*, *38*, L06106, doi:10.1029/2011GL046873.
- Subbotin, D., Y. Shprits, and B. Ni (2010), Three-dimensional VERB radiation belt simulations including mixed diffusion, *J. Geophys. Res.*, *115*, A03205, doi:10.1029/2009JA015070.
- Subbotin, D. A., and Y. Y. Shprits (2009), Three-dimensional modeling of the radiation belts using the Versatile Electron Radiation Belt (VERB) code, *Space Weather*, *7*, S10001, doi:10.1029/2008SW000452.
- Summers, D., R. M. Thorne, and F. Xiao (1998), Relativistic theory of wave-particle resonant diffusion with application to electron acceleration in the magnetosphere, *J. Geophys. Res.*, *103*, 20,487–20,500, doi:10.1029/98JA01740.
- Summers, D., B. Ni, and N. P. Meredith (2007), Timescales for radiation belt electron acceleration and loss due to resonant wave particle interactions: 2. Evaluation for VLF chorus, ELF hiss, and EMIC waves, *J. Geophys. Res.*, *112*, A04207, doi:10.1029/2006JA011993.
- Summers, D., B. Ni, N. P. Meredith, R. B. Horne, R. M. Thorne, M. B. Moldwin, and R. R. Anderson (2008), Electron scattering by whistler-mode ELF hiss in plasmaspheric plumes, *J. Geophys. Res.*, *113*, A04219, doi:10.1029/2007JA012678.
- Tao, X., A. A. Chan, J. M. Albert, and J. A. Miller (2008), Stochastic modeling of multidimensional diffusion in the radiation belts, *J. Geophys. Res.*, *113*, A07212, doi:10.1029/2007JA012985.
- Tao, X., J. M. Albert, and A. A. Chan (2009), Numerical modeling of multidimensional diffusion in the radiation belts using layer methods, *J. Geophys. Res.*, *114*, A02215, doi:10.1029/2008JA013826.
- Tao, X., J. Bortnik, J. M. Albert, and R. M. Thorne (2012), Comparison of bounce-averaged quasi-linear diffusion coefficients for parallel propagating whistler mode waves with test particle simulations, *J. Geophys. Res.*, *117*, A10205, doi:10.1029/2012JA017931.
- Thorne, R. M. (1974), A possible cause of dayside relativistic electron precipitation events, *J. Atmos. Terr. Phys.*, *36*, 635–645.
- Thorne, R. M. (2010), Radiation belt dynamics: The importance of wave-particle interactions, *Geophys. Res. Lett.*, *37*, L22107, doi:10.1029/2010GL044990.
- Thorne, R. M., and L. J. Andreoli (1980), Mechanisms for intense relativistic electron precipitation, in *Exploration of the Polar Upper Atmosphere*, edited by C. S. Deehr and J. A. Holtet, p. 381, D. Reidel, Hingham, Mass.
- Thorne, R. M., R. B. Horne, S. A. Glauert, N. P. Meredith, Y. Y. Shprits, D. Summers, and R. R. Anderson (2005a), The influence of wave-particle interactions on relativistic electrons during storms, in *Inner Magnetosphere Interactions: New Perspectives From Imaging*, *Geophys. Monogr. Ser.*, vol. 159, edited by J. Burch, M. Schulz, and H. Spence, pp. 101–112, AGU, Washington, D. C.
- Thorne, R. M., T. P. O'Brien, Y. Y. Shprits, D. Summers, and R. B. Horne (2005b), Timescale for MeV electron microburst loss during geomagnetic storms, *J. Geophys. Res.*, *110*, A09202, doi:10.1029/2004JA010882.
- Tsyganenko, N. A. (1989), A magnetospheric magnetic field model with a warped tail current sheet, *Planet. Space Sci.*, *37*, 5–20, doi:10.1016/0032-0633(89)90066-4.
- Tu, W., X. Li, Y. Chen, G. D. Reeves, and M. Temerin (2009), Storm-dependent radiation belt electron dynamics, *J. Geophys. Res.*, *114*, A02217, doi:10.1029/2008JA013480.
- Turner, D. L., Y. Shprits, M. Hartinger, and V. Angelopoulos (2012a), Explaining sudden losses of outer radiation belt electrons during geomagnetic storms, *Nat. Phys.*, *8*, 208–212, doi:10.1038/NPHYS2185.
- Turner, D. L., S. K. Morley, Y. Miyoshi, B. Ni, and C.-L. Huang (2012b), Outer radiation belt flux dropouts: Current understanding and unresolved questions, in *Dynamics of the Earth's Radiation Belts and Inner Magnetosphere*, *Geophys. Monogr. Ser.*, edited by D. Summers et al., pp. 195–212, AGU, Washington, D. C.
- Turner, D. L., V. Angelopoulos, Y. Shprits, A. Kellerman, P. Cruce, and D. Larson (2012c), Radial distributions of equatorial phase space density for outer radiation belt electrons, *Geophys. Res. Lett.*, *39*, L09101, doi:10.1029/2012GL051722.
- Ukhorskiy, A. Y., B. J. Anderson, P. C. Brandt, and N. A. Tsyganenko (2006), Storm time evolution of the outer radiation belt: Transport and losses, *J. Geophys. Res.*, *111*, A11503, doi:10.1029/2006JA011690.
- Vampola, A. L., and A. Korth (1992), Electron drift echoes in the inner magnetosphere, *Geophys. Res. Lett.*, *19*(6), 625–628, doi:10.1029/92GL00121.
- Vampola, A. L., J. V. Osborne, and B. M. Johnson (1992), CRRES magnetic electron spectrometer AFGL-701-5A (MEA), *J. Spacecr. Rockets*, *29*, 592–595, doi:10.2514/3.25504.

- Varotsou, A., D. Boscher, S. Bourdarie, R. B. Horne, S. A. Glauert, and N. P. Meredith (2005), Simulation of the outer radiation belt electrons near geosynchronous orbit including both radial diffusion and resonant interaction with Whistler-mode chorus waves, *Geophys. Res. Lett.*, *32*, L19106, doi:10.1029/2005GL023282.
- Varotsou, A., D. Boscher, S. Bourdarie, R. B. Horne, N. P. Meredith, S. A. Glauert, and R. H. Friedel (2008), Three-dimensional test simulations of the outer radiation belt electron dynamics including electron-chorus resonant interactions, *J. Geophys. Res.*, *113*, A12212, doi:10.1029/2007JA01286.
- Van Allen, J. A. (1959), The geomagnetically trapped corpuscular radiation, *J. Geophys. Res.*, *64*, 1683–1689.
- Van Allen, J. A., and L. A. Frank (1959), Radiation around the Earth to a radial distance of 107,400 km, *Nature*, *183*, 430–434.
- Walt, M. (1994), *Introduction to Geomagnetically Trapped Radiation*, Cambridge Univ. Press, Cambridge, U. K.
- Woodfield, E. E., R. B. Horne, S. A. Glauert, J. D. Menietti, and Y. Y. Shprits (2014), The origin of Jupiter's outer radiation belt, *J. Geophys. Res. Space Physics*, *119*, 3490–3502, doi:10.1002/2014JA019891.
- Wrenn, G. L. (1995), Conclusive evidence for internal dielectric charging anomalies on geosynchronous communications spacecraft, *J. Spacecr. Rockets*, *32*, 514–520.
- Wrenn, G. L., D. J. Rodgers, and K. A. Ryden (2002), A solar cycle of spacecraft anomalies due to internal charging, *Ann. Geophys.*, *20*, 953–956.
- Yu, Y., J. Koller, and S. K. Morley (2013), Quantifying the effect of magnetopause shadowing on electron radiation belt dropouts, *Ann. Geophys.*, *31*, 1929–1939.
- Zhao, H., and X. Li (2013), Modeling energetic electron penetration into the slot region and inner radiation belt, *J. Geophys. Res. Space Physics*, *118*, 6936–6945, doi:10.1002/2013JA019240.